Feasibility of Quantitative Magnetic Resonance Fingerprinting in Ovarian Tumors for T_1 and T_2 Mapping in a PET/MR Setting

Joshua D. Kaggie[ID], Surrin Deen, Dimitri A. Kessler, Mary A. McLean[ID], Guido Buonincontri[ID], Rolf F. Schulte, Helen Addley, Evis Sala, James Brenton, Martin J. Graves, and Ferdia A. Gallagher

Abstract—**Multiparametric magnetic resonance imaging (MRI) can be used to characterize many cancer subtypes including ovarian cancer. Quantitative mapping of MRI relaxation values, such as T_1 and T_2 mapping, is promising for improving tumor assessment beyond conventional qualitative T_1- and T_2-weighted images. However, quantitative MRI relaxation mapping methods often involve long scan times due to sequentially measuring many parameters. Magnetic resonance fingerprinting (MRF) is a new method that enables fast quantitative MRI by exploiting the transient signals caused by the variation of pseudorandom sequence parameters. These transient signals are then matched to a simulated dictionary of T_1 and T_2 values to create quantitative maps. The ability of MRF to simultaneously measure multiple parameters, could represent a new approach to characterizing cancer and assessing treatment response. This feasibility study investigates MRF for simultaneous T_1, T_2, and relative proton density (rPD) mapping using ovarian cancer as a model system.**

Index Terms—**Cancer applications, clinical imaging, imaging techniques, magnetic resonance imaging (MRI), oncology, ovarian cancer.**

I. INTRODUCTION

OVARIAN Cancer is the second leading cause of death from gynaecologic cancers [1]. Imaging methods,

including magnetic resonance imaging (MRI), positron emission tomography (PET), and SPECT seek to improve the identification of tumor subtypes as well as their response to treatment. Current clinical MRI methods cannot characterize all tumor subtypes, and therefore better methods must be found in order to create more specific disease biomarkers.

Clinical MR imaging acquires multiple images with different approaches to generate contrast and are usually assessed qualitatively. Contrast on MR imaging is based on differences in magnetic resonance parameters in tissue, such as longitudinal T_1 relaxation, transverse T_2 relaxation, and relative proton density (rPD). Multiple images with different weightings are obtained by varying the acquisition, including parameters, such as repetition time (TR) and flip angle (FA). Although the contrast that is generated is qualitative, contrast is highly dependent on operator specifications, which can complicate the interpretation at multiple centers. In order for the results to be more repeatable and representative of the underlying biological factors that control signal, quantitative MR mapping is essential.

Quantitative mapping of MRI relaxation values is promising for improving tumor diagnosis, for monitoring of disease progression, and for assessment of treatment response beyond simple qualitative assessments [2], [3]. However, traditional quantitative imaging can be inefficient, requiring multiple serial acquisitions from which a single quantitative map can be derived [4]. The measurement of multiple MR parameters is almost always time-consuming and is particularly challenging in moving regions such as the abdomen.

Magnetic resonance fingerprinting (MRF) [4] has recently been introduced, as a novel acquisition and reconstruction strategy to overcome these challenges and time-constraints, with the potential to be used for clinical imaging. MRF could improve the speed and accuracy of PET/MRI parameter quantitation for cancer imaging [5]. MRF in prostate, abdomen, and brain cancer has shown nearly double the T_1 values when compared to normal-appearing tissue, and T_2 differences as large as 70% have been demonstrated between low and high grade tumors [6]–[8].

MRF enables fast, simultaneous, and efficient multiparametric mapping by exploiting the transient signals produced from the variation of pseudo-random sequence parameters. These generated transient signal evolutions or "fingerprints" are unique for different tissues and are dependent on the

various magnetic resonance properties of the tissue. After data acquisition, the signals are matched to a simulated dictionary including (but not limited to) a range of T_1 and T_2 values to create quantitative maps. The rPD is the scaling factor used to match the simulated signal evolution with the measured signal.

The aim of this paper was to assess the feasibility of using MRF for simultaneous T_1, T_2, and rPD mapping of ovarian cancer for the first time. We investigated if the addition of multiparametric MRF to conventional MRI measurements could provide information for the characterization of ovarian masses.

II. MATERIALS AND METHODS

A. Phantom Measurements

MRF and standard relaxation mapping data were obtained from the ISMRM/NIST phantom [9] to assess the accuracy of T_1 and T_2 measurements. Phantom data were obtained on a 3.0 T PET/MR (GE Healthcare, Waukesha, WI, USA) and a standard 3.0 T MR system (MR750, GE Healthcare, Waukesha, WI, USA) using single-channel body coils. Regions-of-interest (ROI) were created from the vials in either the T_1 or T_2 slice of the phantom.

1) Standard T_1 Mapping: Variable FA (VFA) T_1 maps were obtained with a 3-D fast gradient echo sequence with: matrix $= 192 \times 192 \times 72$, field-of-view (FOV) $= 380 \times 380 \times 216$ mm^3, FAs $= 2°$, $5°$, $8°$, $12°$, $15°$, $20°$, TR $= 4.96$ ms, echo time (TE) $= 2.1$ ms, and bandwidth $= \pm 94$ kHz. The T_1 maps were created using linear least-squares fit of the obtained signals using the DESPOT1 method [10], using DICOM images and custom MATLAB code (MathWorks Foundation, Massachusetts, USA).

2) Standard T_2 Mapping: T_2 maps were obtained with a multislice 2-D multiple echo spin echo (MESE) sequence using the following parameters: matrix $= 192 \times 192 \times 21$, FOV $= 380 \times 380 \times 168$ mm^3, matrix $= 192 \times 192 \times 21$, slice thickness $= 3$ mm, slice spacing $= 5$ mm, FA $= 90°$, TR $= 1500$ ms, TEs $= 7, 14, 21, 28, 35, 42, 49, 56$ ms, and bandwidth $= \pm 47$ kHz. The T_2 maps were created using a log-linear-least-squares fit with custom MATLAB code.

3) MRF T_1 and T_2 Mapping: ISMRM/NIST phantom experiments were used to validate MRF on the PET/MR and on the standard MRI system. MRF was repeated on the standard system with follow-ups after an hour and a day, and with three frame lengths to measure these effects on T_1 and T_2 measurements.

A baseline phantom measurement was performed on the standard 3.0 T system, using an initial inversion pulse, and a 38 cm FOV, like the *in vivo* MRF. MRF acquisitions included baseline (=979), 489 ($\approx 1/2 * 979$) or 244 ($\approx 1/2 * 979$) frames with the initial values of the lists [9], [11] in Fig. 1(b) to assess the effect of frame reduction on mapping accuracy. The baseline scan was repeated after an hour and after a week. The same baseline acquisition was obtained using the PET/MR. The temperature of the standard system was 18° for baseline, 17° for one-week follow-up, and 19° for the PET/MR.

In order to find the optimal rank for singular value decomposition (SVD) compression [12] of the dictionary, the data were reconstructed with ranks between 1 and 20. An optimal SVD rank was determined when the T_1 and T_2 difference was less than 1% with the values at SVD rank ≥ 16.

B. In Vivo Imaging

Patient images were acquired on a standard 3.0 T MRI system using a 32-channel abdominal coil. All patients were imaged in the supine position. The MRI protocol consisted of standard qualitative clinical sequences followed by a 2-D steady-state-free precession (SSFP) MRF sequence [4].

In vivo MRF data were acquired using 979 frames with spiral *k*-space interleafs [Fig. 1(a) and (b)]. Each spiral was rotated by the golden-angle for each of 89 interleafs, following which the 89 spirals were then repeated 11 times to fill 979 frames. The golden-angle interleafs enabled the TR and FA lists used to match the values in [9] and [11]. A slice-selective inversion pulse was used prior to FA and TR list variation. Further sequence parameters were: FOV $= 380 \times 380$ mm^2; matrix $= 192 \times 192$; voxel size $= 2.0 \times 2.0 \times 3.0$ mm^3; slice thickness $= 3.0$ mm; slice spacing $= 1.0$ mm; sampling bandwidth $= \pm 250$ kHz; TE $= 1.8$ ms; and acquisition time $= 15$ s/slice, with 18–22 slices per patient, for a total scan time between 4.5 and 5.5 min. The maximum gradient strength per spiral was 17 mT/m and the maximum slew rate was 62 T/m/s. The gradient strength was limited to low values to ensure that a large FOV would be obtained to cover the whole abdomen.

T_1 and T_2 values for the three tumor types were calculated from ROIs drawn on four consecutive slices. Mean relaxation values for the post-treatment subject were determined from ROIs on eight consecutive slices.

C. MRF Dictionary Simulation

Dictionary simulations [Fig. 1(c)] of the signal evolution from an SSFP acquisition scheme were performed using the extended phase graph formalism [5]. The ranges and incremental (step-size) changes of the T_1 and T_2 values that were included in the dictionary are listed in Table I. The range was chosen to represent both short relaxation times, which occur in dense and fatty tissue, and high relaxation times, which occur in fluid regions such as ascites. The increments were chosen to be smaller near short relaxation times, where the increments are a larger percentage change for each dictionary value.

Three temporally adjacent dictionary values were summed for the final dictionary creation, such that a three-frame sliding window reconstruction and matching technique could be used [13]. This process is possible due to the linearity property of the Fourier transformation, which preserves information under linear transformation. The sliding window increased the signal-to-noise and reduced the undersampling artifact from each frame, which was necessary for accurate matching.

D. MRF Reconstruction

MRF data were collected using an under-sampled spiral acquisition that resulted in 979 under-sampled images

TABLE I
RANGES AND INCREMENTAL CHANGES FOR $T1$ AND $T2$

Parameter	Range (ms)	Increment (ms)
T1	10 – 400	10
	400 - 4000	20
T2	2 - 20	1
	20 - 400	2
	400 - 2500	20

TABLE II
DIFFERENCE WITH BASELINE (MEAN ± STDDEV)

	$\Delta T_1/T_{1,Baseline}$ (%)	$\Delta T_2/T_{2,Baseline}$ (%)
Published NIST	-28 ± 16	-38 ± 34
T_1-VFA or T_2-MESE	25 ± 68	-39 ± 14
PET/MR	26 ± 38	17 ± 32
Baseline (979 Frames)	0 ± 0	0 ± 0
Repeat, 1 Hour	-4 ± 19	0.2 ± 3.9
Repeat, 1 Week	7 ± 19	-9 ± 19
½ (=489) Frames	3 ± 36	2 ± 11
¼ (=244) Frames	-1 ± 5	-18 ± 24

per slice. The MRF data were reconstructed using a regridding algorithm to an interpolated Cartesian *k*-space before a fast Fourier transfer (FFT), and used a three frame sliding window [13]. Image reconstruction and dictionary matching was parallelized to increase reconstruction efficiency, which was performed on 48 CPU cores using 400 gigabytes of RAM. After reconstruction of the images from each coil channel, the channels were combined using adaptive coil combination on the average of the time frames [14].

MRF uses a relatively simple pattern recognition algorithm to identify the tissue and its corresponding properties in each voxel. The inner products between the normalized measured signal evolution of each voxel and each normalized dictionary entry are calculated. The dictionary entry returning the maximum value of the inner product is taken as the best representation of the acquired signal evolution. The respective T_1 and T_2 values are consequently assigned to the voxel. The rPD is calculated as the scaling factor used to match the dictionary simulation with the measured signal evolution.

E. SVD Compression

MRF benefits from dimensionality reduction techniques that reduce both the size of the dictionary and of the stored images. Dimensionality reduction enables easier long term storage and faster computation for dictionary matching [12]. SVD is a dimensionality reduction method (or a "principal component analysis" method) that seeks to reduce the number of signal features. SVD performs a linear mapping of the data to a lower dimensional space while maximizing the variance of the reduced set of features. For MRF, both the dictionary and undersampled images are reduced ("compressed" or "factored"), using the SVD decomposition weights that were determined during dictionary compression [12].

Multiple singular vector lengths (or "ranks") were investigated by varying the rank between 1 and 20 for the phantom measurements in order to investigate the variability that is introduced with the SVD compression. For the *in vivo* measurements, rank 16 was used based on the phantom measurement error being lower than 1%.

F. In Vivo Imaging

Four patients were imaged: one borderline serous tumor and three high-grade serous ovarian cancers (HGSOCs). One HGSOC had extensive ascites, and one HGSOC was imaged

TABLE III
MEAN RELAXATION VALUES OF DIFFERENT TUMOR TYPES

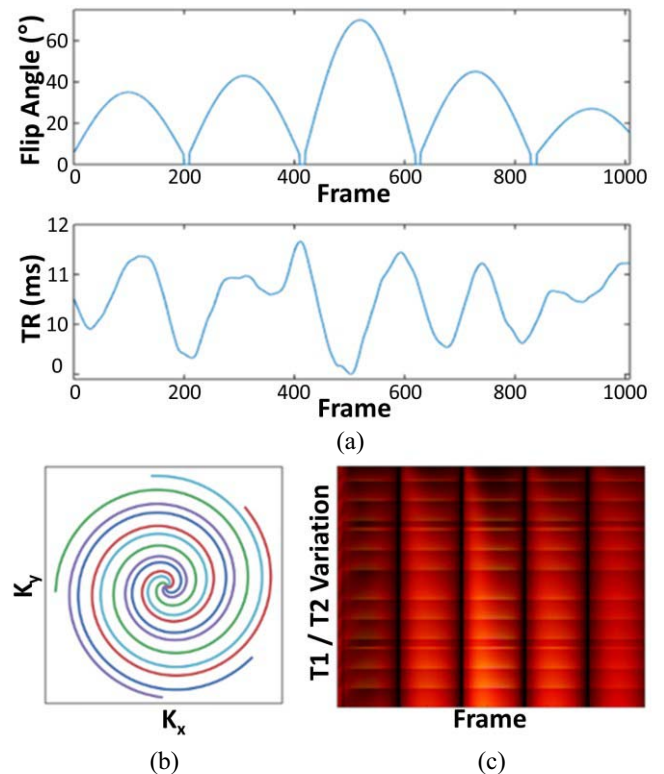| Tumour	T1 (ms)	T2 (ms)
Borderline serous	2465 ± 101	225 ± 34
HGSOC	1975 ± 191	94 ± 15
HGSOC with ascites	1621 ± 46	174 ± 26
HGSOC post treatment	1059 ± 55	116 ± 12

Fig. 1. (a) FA and TR list used during acquisition and simulation. (b) Five spokes showing the *k*-space acquisition with golden angle spiral interleaves. (c) Sample dictionary of simulated signals showing the intensity of the MRF signal for each *k*-space spiral acquisition (frame), for different TRs and FAs.

post chemotherapy with no histological evidence of remaining cancer. All data were acquired with informed consent and local ethical approval.

III. RESULTS

A. Phantom

The ISMRM/NIST phantom T_1 and T_2 values had <10% mean difference between the ratio of the baseline and the PET/MR, 1-h repeat, 1-week repeat, and reduced frame (1/2 and 1/4 length) maps (Fig. 2, Table II). The T_2-MESE measurements underestimated the T_2 by nearly 40% for the ~600 ms phantom vial but had <10% error between 20 and 160 ms. The T_1-VFA measurements overestimated T_1 values above 500 ms by > 60% and could not be fitted below 20 ms.

The SVD rank affected T_2 more than T_1, with larger effects on lower T_1 and T_2 values (Fig. 3). A rank of one resulted in no T_1 or T_2 images. A rank of two enabled large T_1 values (>0.8 s) to be matched within 10% of their rank 20 value, while lower T_1 values required a rank of 11 or higher for similar differences. Similarly, T_2 values >0.5 s were within 20% of their final value above rank 3, within 5% of their final value above rank 11, and within 1% above rank 16.

B. In Vivo

Dictionary simulation was performed in 45 min. The abdominal images obtained with the 32-channel coil required 3.5 h for non-Cartesian reconstruction and matching, per subject.

The generated T_1, T_2, and rPD maps of the four patients are shown in Fig. 4. The mean T_1 and T_2 values and their standard deviations (SDs) estimated from the ROIs for each tumor type are listed in Table III.

The borderline serous ovarian tumor had a higher T_1 value than the two HGSOC untreated lesions, which was discernable on the MRF maps. Mean T_1 and T_2 relaxation times of the borderline tumor were longer by ~20% and ~58%, respectively, when compared with the two pretreatment HGSOC tumors. The treated patient, with no evidence of remaining tumor, demonstrated lower T_1 and T_2 values from the other two HGSOC patients by 50%–150% for T_1 and by 33%–50% for T_2.

IV. DISCUSSION

This proof-of-principle study has demonstrated the feasibility of using MRF for fast quantification of relaxation parameters in ovarian cancer for the first time. The quantitative MRF maps generated in this proof-of-concept work have demonstrated variations in T_1 and T_2 that could be assessed for further characterization of tumors in future studies.

A. Phantom

The baseline (979 frame) MRF demonstrated had <5% T_1 differences from 1/2 and 1/4 frame experiments, which suggests that the parameter list can be reduced without loss of accuracy. A reduction in the list lengths would proportionally reduce the time required for acquisition and dictionary matching. Interestingly, the 1/2 and 1/4 frame lists were closer to published NIST value for T_2, which, if confirmed in more experiments, could be a result of increasing the weight of signals affected by the initial inversion pulse before the list.
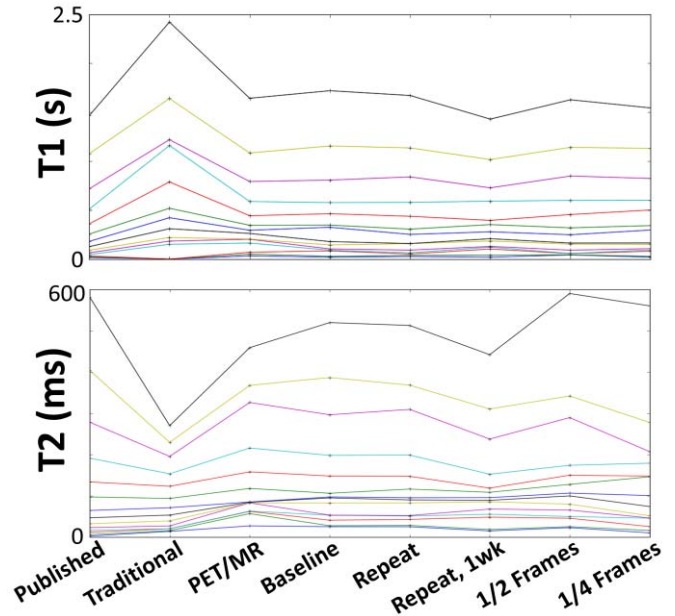

Fig. 2. T_1 and T_2 values measured in the ISMRM/NIST phantom vials (of the T_1-slice and T_2-slice of the phantom, respectively). Each horizontal line corresponds to a single vial, which would be constant with repeatable and reproducible conditions. The labels indicate values obtained from: *Published* values in the NIST manual; *Traditional* quantification with standard T_2 multi-tiecho spin echo (ME*SE*) or T_1 VFA mapping; using the *PET/MR*; on the clinical system (*Baseline*), *Repeat*ed after an hour and after 1 *week*, and using a reduced number of *Frames* (1/2 or 1/4) when compared with baseline (frames = 979).
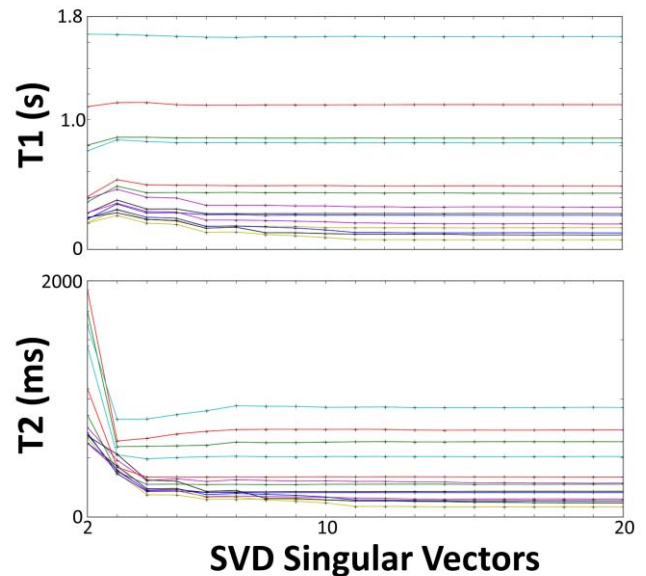

Fig. 3. T_1 and T_2 values measured in the ISMRM/NIST phantom with the number of singular vectors for SVD compression (= rank) varied between 2 and 20 before matching. Each horizontal line represents a static T_1 or T_2 value. Both plots show values from vials in the T_2-slice. Longer T_1 and T_2 values (>0.5 s) are accurate with rank > 3, while shorter relaxation values require rank > 16 to have less than 1% difference with rank 20.

The MRF quantitative maps were closer to the accepted ISMRM/NIST values for a wider range of T_1 and T_2 values when compared to conventionally acquired quantitative maps in the ISMRM/NIST phantom (Fig. 2). The short TR
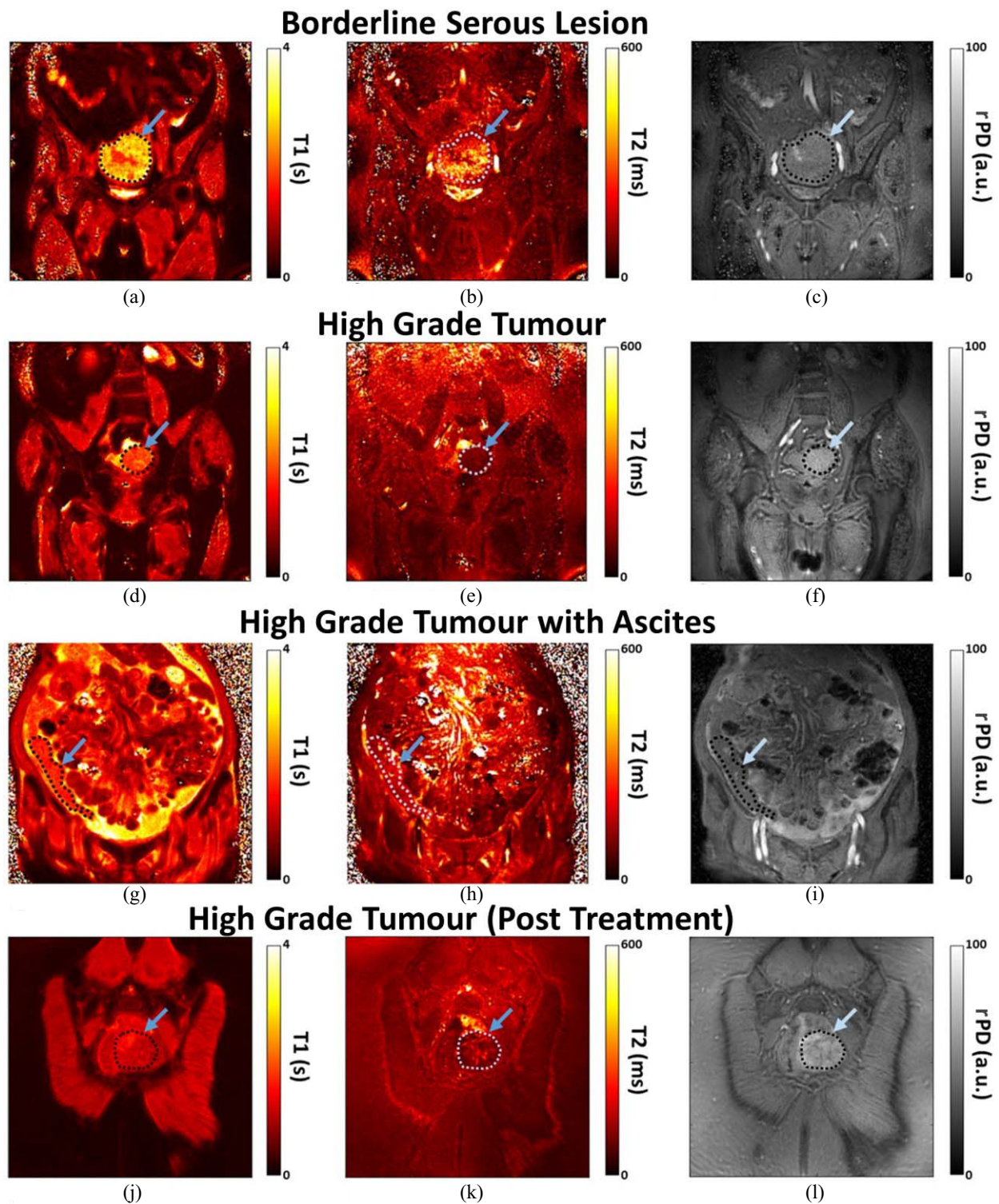
Fig. 4. Coronal T_1, T_2, and PD quantitative maps of the four patients with (a)–(c) borderline serous and (d)–(l) high grade tumors. One of the HGSOC tumors had extensive ascites, and the HGSOC patient who had treatment had no histological evidence of remaining carcinoma (j)–(l). The T_2 images (b), (e), (h), and (k) are shown with a maximum scale of 600 ms, although the dictionary was created up to values of 2.5 s.

(=1500 ms) was a likely source of error for vials with long T_1 values during conventional T_2 mapping. Nonuniform B_1+ fields were a source of error for conventional T_1 mapping. The MRF maps were not accurate for T_1 or T_2 values below 30 ms, which resulted in nearly similar values near 20 ms for four vials, despite the increased resolution of simulated T_1 and T_2 values. These short T_2 ranges are important for fat quantitation, which has fast relaxation. Simulations are required to determine how to optimize for these values, which may require dramatically changing the TR or FA lists.

The compression of the images was performed at rank 16 for *in vivo* assessment because the phantom differences between rank 16 and higher rank were less than 1%. While increasing the rank would ideally result in higher precision, the compressed images beyond the first sixteen have noise-like appearances, suggesting negligible benefit with their inclusion. This noise-like appearance at high rank is likely due to an insufficient *in vivo* signal-to-noise ratio from the use of large abdominal coils, the presence of multiple tissue types, and motion artifact.

This is the first demonstration of ISMRM/NIST phantom MRF measurements on a PET/MR system. Previous work with MRF on a PET/MR has not assessed the phantom measurement accuracy [15].

B. In Vivo

This feasibility study was a first abdominal MRF experiment on our system, so acquisition parameters were conservative. We used a conservative maximum gradient strength and slew rate to ensure sufficient signal-to-noise for accurate matching. *In vivo* mapping has challenges not present in phantom measurements, such as requiring a larger FOV, increasing receiver channel numbers, introducing artifact from respiratory motion, and increasing B_0 and B_1 field nonuniformity. Previous MRF of the abdomen was shown by Chen *et al.* [8], who used 2500 spiral arms (frames) for a single 5-mm thick slice, with the FOV = 44 cm, and with each frame rotated by 7.5°. Our *in vivo* work used 979 frames with golden angle spiral rotations and acquired 18-22 slices.

These results are promising in demonstrating the feasibility of MRF for quantitative pelvis and abdominal MRI. This feasibility study does not have sufficient numbers to demonstrate clinical benefit due to the limited patient sample size. Therefore, these preliminary results need to be validated in a larger cohort to assess the robustness of the results. This approach can be used to validate MRF as a fast and reliable alternative to the time-consuming gold-standard methods to acquire this data. Increased MRF resolution could be used to detect smaller tumor lesions in the future.

Ascites is difficult with traditional MRI methods because conductive ascitic fluid introduces standing waves that attenuate the radiofrequency fields, resulting in signal loss [16], [17]. Ascites-related loss is not visible in the maps of Fig. 4(g)–(i). Initial experiments with a reduced T_1 and T_2 parameter range [9] resulted in T_2 values that were at the upper limit of the dictionary, so the dictionary range was extended (Table I) to map these compartments. Ascites map reconstruction did not otherwise present challenges different from the other subject maps.

Biological variation is visible on the MRF images [Fig. 4(a)–(c) and (j)–(l)], which is important for future work evaluating intratumoral heterogeneity: HGSOC is known to be very heterogeneous, which may be relevant for tumor progression and resistance to therapy [18]. Biological validation of image heterogeneity on histology will be important in future studies. Furthermore, MRF quantitative maps could be used in conjunction with radiomic measurements of tumor heterogeneity once these methods are validated.

Our nominal FOV(=38 cm) was chosen to image the whole abdomen, although was slightly smaller than the abdomen of three patients [Fig. 4(a)–(f) and (j)–(l)]. The maps of Fig. 4(d)–(f) and (j)–(l) do not appear to have image aliasing artifact that could be caused by a small FOV. Aliasing was reduced though the golden angle sampling pattern, which enabled a dense *k*-space that creates a large FOV, and reduces sensitivity to motion artifact [19]. Spiral acquisition regridding to a Cartesian *k*-space also enabled a large reconstructed FOV due to the interpolation of intermediate *k*-space values from coils with limited sensitivity regions [20], which acts similarly to other coil acceleration methods. Dictionary matching also reduced image aliasing, as the coils with the highest signal-to-noise contribute more than aliased, distant coils.

Respiratory artifact is not apparent on these images. Although the pelvis is subject to respiratory motion, these images were acquired with free-breathing during the 4-min scan. The pelvis is lower than other abdominal areas, and therefore is less sensitive to motion than the upper abdomen. MRF is relatively insensitive to motion because pattern matching occurs when a voxel is static for enough frames. It remains to be determined whether fewer frames reduces motion artifact due to faster acquisition speeds, or a larger number of frames reduces artifact due to increased signal averaging and samples that can be matched.

The original MRF paper by Ma *et al.* [4] used 32-coil channels, and acquired a single-slice matrix of 128×128 with 1000 frames. This paper acquired twice as much data per slice, while including more slices, and involved a lengthy 3–4 h reconstruction, which does not include the dictionary creation time. Due to the large number of simulated and imaging parameters, the data was reconstructed in chunks by matching groups of voxels and slices independently. A 3-frame sliding window [13] increased the reconstruction time and memory requirements. The 3-frame sliding window was necessary to reduce the variability on the *in vivo* T_2 maps, which otherwise were very noisy when reconstructed with a single frame.

In addition to relaxation time measurements, the MRF methodology could be combined with other tissue property measurements, such as diffusion and perfusion, to gain more information for an improved classification of tumor masses. Combining metabolic information gained from uptake of the glucose analog, 2-deoxy-2-[^{18}F]-fluoro-D-glucose (^{18}F-FDG) on PET [21], [22] with the anatomical and functional information gained from MRI has a potential to improve the detection and characterization of tumors as well as assessment of treatment response.

REFERENCES

[1] J. Ferlay *et al.*, "Cancer incidence and mortality worldwide: Sources, methods and major patterns in GLOBOCAN 2012," *Int. J. Cancer*, vol. 136, no. 5, pp. E359–E386, 2015.

[2] J. S. Carter *et al.*, "Quantitative multiparametric MRI of ovarian cancer," *J. Magn. Reson. Imaging*, vol. 38, no. 6, pp. 1501–1509, 2013.

[3] H.-M. Li *et al.*, "Quantitative dynamic contrast-enhanced MR imaging for differentiating benign, borderline, and malignant ovarian tumors," *Abdominal Radiol.*, vol. 43, no. 11, pp. 1–10, 2018.

[4] D. Ma *et al.*, "Magnetic resonance fingerprinting," *Nature*, vol. 495, pp. 187–192, Mar. 2013.

[5] K. M. Ropella-Panagis, N. Seiberlich, and V. Gulani, "Magnetic resonance fingerprinting: Implications and opportunities for PET/MR," *IEEE Trans. Radiat. Plasma Med. Sci.*, to be published. doi: 10.1109/TRPMS.2019.2897425.

[6] C. Badve *et al.*, "MR fingerprinting of adult brain tumors: Initial experience," *Amer. J. Neuroradiol.*, vol. 38, no. 3, pp. 492–499, 2017.

[7] A. C. Yu *et al.*, "Development of a combined MR fingerprinting and diffusion examination for prostate cancer," *Radiology*, vol. 283, no. 3, pp. 729–738, 2017.

[8] Y. Chen *et al.*, "MR fingerprinting for rapid quantitative abdominal imaging," *Radiology*, vol. 279, no. 1, pp. 278–286, 2016.

[9] Y. Jiang *et al.*, "Repeatability of magnetic resonance fingerprinting T1 and T2 estimates assessed using the ISMRM/NIST MRI system phantom," *Magn. Reson. Med.*, vol. 78, no. 4, pp. 1452–1457, 2017.

[10] S. C. Deoni, "High-resolution T1 mapping of the brain at 3T with driven equilibrium single pulse observation of T1 with high-speed incorporation of RF field inhomogeneities (DESPOT1-HIFI)," *J. Magn. Reson. Imaging*, vol. 26, no. 4, pp. 1106–1111, 2007.

[11] Y. Jiang, D. Ma, N. Seiberlich, V. Gulani, and M. A. Griswold, "MR fingerprinting using fast imaging with steady state precession (FISP) with spiral readout," *Magn. Reson. Med.*, vol. 74, no. 6, pp. 1621–1631, 2015.

[12] D. F. McGivney *et al.*, "SVD compression for magnetic resonance fingerprinting in the time domain," *IEEE Trans. Med. Imag.*, vol. 33, no. 12, pp. 2311–2322, Dec. 2014.

[13] X. Cao *et al.*, "Robust sliding-window reconstruction for accelerating the acquisition of MR fingerprinting," *Magn. Reson. Med.*, vol. 78, no. 4, pp. 1579–1588, 2017.

[14] D. O. Walsh, A. F. Gmitro, and M. W. Marcellin, "Adaptive reconstruction of phased array MR imagery," *Magn. Reson. Med.*, vol. 43, no. 5, pp. 682–690, 2000.

[15] F. Knoll *et al.*, "Joint MR-PET reconstruction using a multi-channel image regularizer," *IEEE Trans. Med. Imag.*, vol. 36, no. 1, pp. 1–16, Jan. 2017.

[16] M. J. Graves and D. G. Mitchell, "Body MRI artifacts in clinical practice: A physicist's and radiologist's perspective," *J. Magn. Reson. Imag.*, vol. 38, no. 2, pp. 269–287, 2013.

[17] M. M. Barth, M. P. Smith, I. Pedrosa, R. E. Lenkinski, and N. M. Rofsky, "Body MR imaging at 3.0 T: Understanding the opportunities and challenges," *Radiographics*, vol. 27, no. 5, pp. 1445–1462, 2007.

[18] R. F. Schwarz *et al.*, "Spatial and temporal heterogeneity in high-grade serous ovarian cancer: A phylogenetic analysis," *PLoS Med.*, vol. 12, no. 2, 2015, Art. no. e1001789.

[19] S. Winkelmann, T. Schaeffter, T. Koehler, H. Eggers, and O. Doessel, "An optimal radial profile order based on the golden ratio for time-resolved MRI," *IEEE Trans. Med. Imag.*, vol. 26, no. 1, pp. 68–76, Jan. 2007.

[20] K. P. Pruessmann, M. Weiger, M. B. Scheidegger, and P. Boesiger, "SENSE: Sensitivity encoding for fast MRI," *Magn. Reson. Med.*, vol. 42, no. 5, pp. 952–962, Nov. 1999.

[21] M. A. Queiroz *et al.*, "PET/MRI and PET/CT in advanced gynaecological tumours: Initial experience and comparison," *Eur. Radiol.*, vol. 25, no. 8, pp. 2222–2230, 2015.

[22] C. Spick, K. Herrmann, and J. Czernin, "18F-FDG PET/CT and PET/MRI perform equally well in cancer: Evidence from studies on more than 2,300 patients," *J. Nucl. Med.*, vol. 57, no. 3, pp. 420–430, 2016.